Earth and Planetary Science Letters 560 (2021) 116794

Contents lists available at ScienceDirect

Earth and Planetary Science Letters

www.elsevier.com/locate/epsl

The micrometeorite flux at Dome C (Antarctica), monitoring the accretion of extraterrestrial dust on Earth

J. Rojas [a,*], J. Duprat [b,a], C. Engrand [a], E. Dartois [c], L. Delauche [a], M. Godard [a,c], M. Gounelle [b], J.D. Carrillo-Sánchez [d,e], P. Pokorný [d,f], J.M.C. Plane [g]

[a] Université Paris-Saclay, CNRS/IN2P3, IJCLab, 91405 Orsay, France
[b] IMPMC, CNRS-MNHN-Sorbonne Universités, UMR7590, 57 rue Cuvier, 75005 Paris, France
[c] ISMO, CNRS, Univ. Paris Saclay, Bât 520, 91405 Orsay, France
[d] Department of Physics, Catholic University of America, 620 Michigan Ave., N.E., Washington, DC 20064, USA
[e] ITM Physics Laboratory, NASA Goddard Space Flight Center, Code 675, 8800 Greenbelt Rd., Greenbelt, MD 20771, USA
[f] Astrophysics Science Division, NASA Goddard Space Flight Center, Code 667, 8800 Greenbelt Rd., Greenbelt, MD, USA
[g] School of Chemistry, Univ. of Leeds, Leeds LS2 9JT, UK

ARTICLE INFO

Article history:
Received 17 September 2020
Received in revised form 21 January 2021
Accepted 29 January 2021
Available online 10 February 2021
Editor: F. Moynier

Keywords:
Antarctic micrometeorites
cosmic spherules
interplanetary dust particles
extraterrestrial flux
atmospheric entry
zodiacal cloud

ABSTRACT

The annual flux of extraterrestrial material on Earth is largely dominated by sub-millimetre particles. The mass distribution and absolute value of this cosmic dust flux at the Earth's surface is however still uncertain due to the difficulty in monitoring both the collection efficiency and the exposure parameter (i.e. the area-time product in m^2.yr). In this paper, we present results from micrometeorite collections originating from the vicinity of the CONCORDIA Station located at Dome C (Antarctica), where we performed several independent melts of large volumes of ultra-clean snow. The regular precipitation rate and the exceptional cleanliness of the snow from central Antarctica allow a unique control on both the exposure parameter and the collection efficiency. A total of 1280 unmelted micrometeorites (uMMs) and 808 cosmic spherules (CSs) with diameters ranging from 30 to 350 µm were identified. Within that size range, we measured mass fluxes of 3.0 µg.m^{-2}.yr^{-1} for uMMs and 5.6 µg.m^{-2}.yr^{-1} for CSs. Extrapolated to the global flux of particles in the 12-700 µm diameter range, the mass flux of dust at Earth's surface is $5,200 \pm^{1500}_{1200}$ tons.yr^{-1} ($1,600 \pm 500$ and $3,600 \pm^{1000}_{700}$ tons.yr^{-1} of uMMs and CSs, respectively). We indicate the statistical uncertainties expected for collections with exposure parameters in the range of 0.1 up to 10^5 m^2.yr. In addition, we estimated the flux of altered and unaltered carbon carried by heated and un-heated particles at Earth's surface. The mass distributions of CSs and uMMs larger than 100 µm are fairly well reproduced by the CABMOD-ZoDy model that includes melting and evaporation during atmospheric entry of the interplanetary dust flux. These numerical simulations suggest that most of the uMMs and CSs originate from Jupiter family comets and a minor part from the main asteroid belt. The total dust mass input before atmospheric entry is estimated at 15,000 tons.yr^{-1}. The existing discrepancy between the flux data and the model for uMMs below 100 µm suggests that small fragile uMMs may evade present day collections, and/or that the amount of small interplanetary particles at 1 AU may be smaller than expected.

Contents

---

[*] Corresponding author.
E-mail address: Julien.Rojas@csnsm.in2p3.fr (J. Rojas).

https://doi.org/10.1016/j.epsl.2021.116794
0012-821X/

1. Introduction

More than a century after the discovery of cosmic spherules in deep-sea sediments (Murray and Renard, 1891), the origin, composition and magnitude of the cosmic dust accretion on Earth is still a matter of debate. Extraterrestrial dust flux studies have been performed before atmospheric entry, while collections at the Earth's surface of both melted and unmelted micrometeorites were achieved in numerous locations such as the deep sea, deserts, sedimentary rocks and the polar ice caps (Yada et al. (2004), and reference therein). Although all these studies demonstrated that the annual extraterrestrial mass input on Earth is essentially carried by sub-millimetre particles, the precise mass distribution of particles down to a few tens of µm and its integrated value at the Earth surface remain uncertain (Plane, 2012). A first reason for these large uncertainties is the difficulty of collecting and identifying, with a well-controlled efficiency, extraterrestrial particles with diameters in the range of a few tens to hundreds of µm. A second reason is the difficulty of inferring a well-quantified exposure parameter (the area-time product, in m^2.yr). In order to provide an accurate constraint on the exposure parameter, that is the area of fall multiplied by the duration of the accumulation, it is mandatory to control both the volume of the host matrix of the particles (sediment, ice, snow, ...) from which the particles are extracted, and its local accumulation rate (in $g.m^{-2}.yr^{-1}$).

We present here results from a long-term collection of extraterrestrial particles performed during the last two decades in the vicinity of the CONCORDIA station located at Dome C, in the central regions of the Antarctic continent. The unique characteristics of Dome C and the specific collection protocol developed for this study allowed an accurate control maintained on both the collection efficiency, specifically in the lowest diameter range where the flux mass contribution was the least constrained, and on the exposure parameter. The comprehensive study presented in this work allows to perform several independent measurements of the absolute flux, and hence to obtain a better constraint on the size distribution of micrometeorites reaching the Earth's surface. We use these data to perform numerical simulations to quantify possible statistical biases impacting the flux estimation; this is done by considering a large range of exposure parameters. Finally, we compare the results obtained with this collection with data from previous studies at the Earth's surface and with observations and model predictions of the flux before atmospheric entry.

The size distribution of cosmic dust in the 10-1000 µm diameter range before atmospheric entry can be inferred using infrared observations of the Zodiacal Cloud (Ade et al., 2014; Hauser et al., 1984; Sykes, 1990), dust detectors in space (Love and Brownlee, 1993) or radar observations (Plane, 2012). During atmospheric entry, part of the flux is vaporized while another part survives as melted and unmelted particles. The complex physico-chemical processes occurring during atmospheric entry can be described using the CABMOD-ZoDy model (Carrillo-Sánchez et al., 2016; Nesvorný et al., 2011; Plane, 2012). In this study, the CABMOD-ZoDy model was updated to take into account the measured mass distribution. The comparison between the data from the CONCORDIA collection and the predictions of the updated CABMOD-ZoDy model allows light to be shed on the evolution of dust from the interplanetary reservoir, through the partially destructive processes at atmospheric entry to final deposition at the Earth's surface.

2. Materials and methods

2.1. Collection of micrometeorites at Dome C

The micrometeorites presented in this work were collected in the vicinity of the French-Italian CONCORDIA station at Dome C (hereafter DC). The station is located 1100 km inland on the high Antarctic plateau, at 75°06'S 123°20'E, 3200 m above sea level (Fig. 1). The specific location of this site offers unique preservation conditions for micrometeorites against aqueous alteration, and anthropic and terrestrial contaminations. To prevent potential anthropic contamination due to activities at the station, samples of snow were extracted in trenches with depths larger than 2 m, corresponding to years prior to 1995, which is the beginning of human presence in that area. The trenches were located several hundreds of meters to a few km upwind from the station. The snow was extracted from the trenches using saws and shovels that were previously cleaned with water and ethanol.

In this work, we derive results from particles extracted from 3 field campaigns that took place during the December-February period (austral summers) 2001-2002, 2005-2006 and 2015-2016. The average temperature in the trench was stable, ranging from −45 °C to −55 °C. The 2001-2002 collection (hereafter DC02) was performed in a 4 m deep trench located about 200 m from the station, at GPS coordinates (75°06′25.5″S 123°20′39.66″E). The snow was extracted from depths ranging from 2.0 to 3.5 m. The 2005-2006 collection (hereafter DC06) was performed in two trenches located at about 1 km from the station. The first trench was at GPS coordinates (75°06′35.46″S 123°20′39.66″E), the second trench was located 100 m from the first one in the SW direction. The extraction depths ranged from 3.3 to 4.3 m. The 2015-2016 collection (hereafter DC16) was performed in a trench located 3 km from the station at GPS coordinates (75°07′29.1″S 123°21′42.6″E), and the snow was extracted from depths ranging from 6.5 to 8.5 meters.

The snow was carried from the trench to the station in 60 litres high-density polyethylene closed barrels, with an average snow-per-barrel weight of about 15-20 kg. The snow was melted using a dedicated stainless-steel melter (Fig. 1) combined with a 35 kW propane gas boiler that gently warmed the stainless-steel tank via an external water bath. The melted snow water was sieved on a 30 µm mesh nylon filter for the DC02 and DC06 collections, and on a 20 µm mesh filter for the DC16 campaign. The filtering was made using gravity without water pumping to avoid putting mechanical stress on micrometeorites. The melter was a closed system

Fig. 1. Left: Location of the CONCORDIA station (Dome C, Antarctica). Centre: View of a trench at Dome C. Right: Monitoring the melting of the snow in the double tank melter for the extraction of micrometeorites.

Table 1
Number (a,b) and mass (c,d) of uMMs and CSs collected in each melt (before collection efficiency correction). Weight of snow in each melt (e) and corresponding exposure parameter S (f, see text). Numbers (g,h) and mass (i,j) of uMMs and CSs per kg of snow. The 4 first rows display data from the selected melts used to infer the absolute value of the flux. The additional set of particles is reported on row 7 (noted Add. Set) and the complete set on row 8 (noted All data) (see text).

	N uMM (a)	N CS (b)	Mass uMM (μg) (c)	Mass CS (μg) (d)	Snow weight (kg) (e)	S (m^2.yr) (f)	N(uMM)/kg of snow (g)	N(CS)/kg of snow (h)	M(uMM)/kg of snow (μg/kg) (i)	M(CS)/kg of snow (μg/kg) (j)
DC06-07	103	89	48	120	681	25.2	0.151	0.131	0.070	0.176
DC06-08	65	123	71	136	835	30.9	0.078	0.147	0.085	0.163
DC06-09	294	116	116	136	903	33.4	0.326	0.128	0.128	0.151
DC06-11	195	–	146	–	1142	42.3	0.171	–	0.128	–
uMMs Dataset #1	657	–	381	–	3561	131.9	0.185	–	0.107	–
CSs Dataset #1	–	328	–	392	2419	89.6	–	0.136	–	0.162
Add. set	623	480	368	647	–	–	–	–	–	–
All data	1280	808	749	1039	–	–	–	–	–	–

and the total weight of melted snow was obtained by measuring the volume of filtered water. The usual exposure of the particles to water was about 10 hours, and in rare cases longer, but always less than 3 days. Each melt was sieved on a single filter and extensive rinsing of the melter walls was performed to ensure maximum recovery of the particles. All filters were subsequently analysed in a dedicated clean room (ISO 7) under a clean hood at CSNSM (Centre de Sciences Nucléaires et de Sciences de la Matière, now IJCLab).

The most recent studies of the snow accumulation rate R_{snow} at Dome C indicate values ranging from 2.6 to 2.8 $g.cm^{-2}.yr^{-1}$ over the last century (Frezzotti et al., 2005; Le Meur et al., 2018). In the present work, we take an average value of $R_{snow} = (2.7 \pm 0.1)$ $g.cm^{-2}.yr^{-1}$. Considering an average mass density of snow of 300 $kg.m^{-3}$, the corresponding dates of fall of the particles range between 1920 and 1980.

We attributed to each melt an exposure parameter S, expressed in m^2.yr (Table 1). S is an area-time product (Peucker-Ehrenbrink et al., 2016) representing the accumulated quantity of snow trapping the particles. It is derived from the mass of snow in a melt M_{melt} (g) and the accumulation rate R_{snow} ($g.m^{-2}.yr^{-1}$) by:

$$S = \frac{M_{melt}}{R_{snow}}$$

The micrometeorite collection efficiency Q was monitored by introducing in the inner tank, before the snow-melting, a given number of coloured terrestrial sand and glass particles of two size ranges: 50-100 μm and 100-400 μm. The colours were different from one melt to another and between the two size ranges in order to identify possible size dependence in the collection efficiency as well as possible mixing between consecutive melts in the case of incomplete rinsing. These coloured particles were recovered and counted during the extraction procedure at CSNSM. The inferred average Q for these two size ranges was found to be $Q = (90 \pm 10)\%$ with no significant variations from one melt to another or between the two size ranges. This high Q was obtained by virtue of the dedicated design and polishing of the melter walls, and the extensive and careful rinsing of the overall apparatus after each melt. We systematically divided the number of micrometeorites recovered per melt by Q.

2.2. *Micrometeorite identification and statistics*

The filters were examined in the clean room at CSNSM under a binocular microscope and particles were manually extracted using dedicated fine brushes. The main contaminants observed in the filters were fibres from polar clothes and gloves, plastic chips from the barrels and from the tools used to extract and transport the snow. These contaminants were easily identified and removed during the filter sorting procedure.

Optical images of all extracted particles were taken and both their longest (a) and shortest (b) dimensions were documented, providing an equivalent diameter, D_{eq}, defined as:

$$D_{eq} = (a \times b \times b)^{\frac{1}{3}}$$

Although the size of the filters' mesh is 30 μm for DC02 and DC06, and 20 μm for DC16, some particles with D_{eq} slightly smaller than the mesh sizes were retrieved due to their non-spherical geometry and/or trapping within the textile fibres present in the filters. After extraction from the filters, all unmelted micrometeorites (uMMs) were fragmented. A fragment was then deposited on a carbon tape mounted on a one-inch aluminium disk for analytical scanning electron microscopy (SEM-EDX). Cosmic spherules (CSs) were mounted on carbon tape without fragmentation. All CS and uMM fragments were analysed with a SEM equipped with secondary and back-scattered electron detectors and an Energy Dispersive X-ray

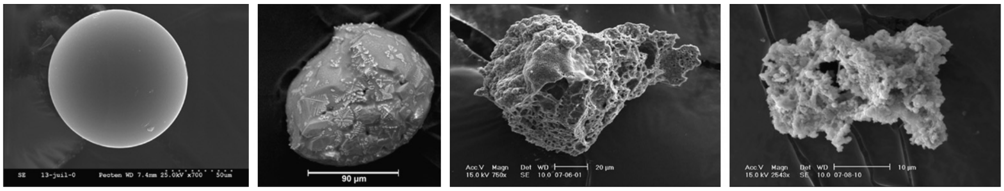

Fig. 2. Cosmic spherules and unmelted micrometeorites from CONCORDIA collection (SEM images). From left to right: glassy cosmic spherule, stony cosmic spherule, partially melted (scoriaceous) micrometeorite, unmelted fine-grained micrometeorite.

spectrometer (EDX) to determine the major elemental composition patterns. Examples of the various kinds of micrometeorites encountered are displayed in Fig. 2.

We performed a comprehensive search for CSs and uMMs contained in the filters of 3 selected melts from the DC06 fieldwork, hereafter referred as DC06-07, DC06-08, DC06-09. We performed a comprehensive search of only uMMs (not CSs) in one additional melt: DC06-11. The total numbers of uMMs and CSs in these selected melts are summarized as dataset #1, in Table 1.

Besides these selected melts in which the particle extraction was exhaustive, we recovered many CSs and uMMs from 19 other melts performed during the DC02, DC06 and DC16 campaigns. The collection protocols from these melts were identical to those of the selected melts. From these 19 additional melts, we extracted 480 CSs and 623 uMMs (see Table 1). The average number of particles per kg of snow in these additional melts was lower than that found in the selected melts mentioned above, due to incomplete scanning of the filters. However, the size distribution of particles within these additional melts was found compatible with that of the selected melts, indicating that there was no significant size bias between the two sets of data (dataset #1 and additional). We used the dataset #1 to infer the absolute value of the fluxes, and the complete set of data (dataset #1 + additional melts) to infer the global size and mass distributions. The global mass influx distributions were then normalized to the absolute values of the flux inferred from the selected melts.

The individual CS masses were estimated assuming an average density of 3.0 g.cm^{-3} (Murrell et al., 1980). The density of an individual uMM depends on the composition and porosity of the particle. Different average densities have been reported for unmelted extraterrestrial particles originating from space-borne, stratospheric and Antarctic collections. In their detailed study of Antarctic micrometeorites, Yada et al. (2004) reported an average density of 1.0 g.cm^{-3} for unmelted particles. The GIADA instrument onboard Rosetta measured an average mass density of 0.795 g.cm^{-3} for cometary dust ejected from 67P-Churyumov-Gerasimenko (Fulle et al., 2016). Individual interplanetary dust particles collected in the stratosphere by NASA (IDPs) exhibit densities ranging from 0.6 up to 4.2 g.cm^{-3} depending on their compact or fluffy nature (Joswiak et al., 2007). The range of densities reported in genuine interplanetary material provides clues for identifying their asteroidal or cometary origin (Consolmagno et al., 2008). Unmelted particles originating from the cometary reservoir most probably have higher porosity, i.e. densities around 0.8-1.0 g.cm^{-3}, while those originating from the asteroidal reservoir have lower porosity and an average density close to that reported for carbonaceous chondrites, i.e. 2.2 g.cm^{-3} (Consolmagno et al., 2008; Flynn and Sutton, 1991; Joswiak et al., 2007; Love et al., 1994). In the following, we considered an average density of 1.5 g.cm^{-3} for uMMs, that is intermediate between these two end-members. This average density is slightly higher than that used by Yada et al. (2004), but in agreement with the fact that we include partially melted grains in the set of uMMs particles. We will return to the discussion of uMM densities when comparing the measurements with the predictions from dynamical simulations (see 4.2).

Despite the high intrinsic Q, the normalized number of particles recovered per kg of snow in each filter exhibits substantial variations (see Table 1). These variations are much larger for uMMs than for CSs and are probably due to uncertainties in the handpicking extraction procedure itself, especially for particles in the lowest size range ($D_{eq} < 50$ µm) that are the most difficult to identify optically. While CSs are straightforward to identify as their spherical shape contrasts with neighbouring particles, the smallest uMMs are more difficult to identify and may escape binocular inspection.

In DC06-07, DC06-08 and DC06-09, 328 CSs were identified with D_{eq} ranging from 20 to 240 µm. The total weight of snow for these 3 melts was 2419 kg, equivalent to $S = 89.6 \pm 3.3$ m^2.yr (Table 1). The average mass of CSs per kg of snow is comparable in the 3 melts ranging from 0.151 µg.kg^{-1} to 0.176 µg.kg^{-1}, with an average value of 0.163 µg.kg^{-1}. The average number of CSs per kg of snow for each melt ranges from 0.128 to 0.147 CS.kg^{-1}, with an average value of 0.135 CS.kg^{-1}.

In DC06-07, DC06-08, DC06-09 and DC06-11 we found 657 uMMs with D_{eq} ranging from 17 to 332 µm. The 4 melts correspond to a total of 3561 kg of snow, i.e. $S = 131.9 \pm 4.9$ m^2.yr. The average mass of uMMs per kg of snow for each melt ranges from 0.070 µg.kg^{-1} to 0.128 µg.kg^{-1}, with an average value of 0.103 µg.kg^{-1}. The average number of uMMs recovered per kg of snow exhibits more pronounced relative variations, from 0.078 to 0.326 uMMs.kg^{-1}. As mentioned before, these large variations in counting are probably due to an incomplete recovery of the smallest particles within given melts. Since the smallest particles do not make a substantial contribution to the mass flux, this incomplete recovery has a limited impact on the inferred total uMMs mass flux.

The percentage of terrestrial grains extracted from the filters varied, depending on the cleanliness of each collection and on the completeness of the extraction. However, it was found to be below 50% in most cases: for melts in which a comprehensive search of all particles was performed, i.e. DC06-07, DC06-08 and DC06-09, it was respectively equal to 28%, 16% and 20%. This high extraterrestrial to terrestrial particle ratio (ET/T ratio) is due to the very low intrinsic abundance in the snow of terrestrial particles with $D_{eq} > 30$ µm; most terrestrial particles reaching the central regions of Antarctica having $D_{eq} < 5$ µm (Delmonte et al., 2004). The variation we observed in the ET/T ratio is thus directly related to contaminations occurring during the collection process itself.

In the results section, we present absolute flux values using the selected melts (dataset #1) comprising 657 uMMs and 328 CSs, and global distributions inferred from the full data set, amounting to 1280 uMMs and 808 CSs.

2.3. Dynamical and atmospheric entry simulations

Recently, Carrillo-Sánchez et al. (2020a, 2020b) combined the Chemical ABlation MODel (CABMOD, Vondrak et al. (2008)) with the Zodiacal Cloud Model (ZoDy, Nesvorný et al. (2010, 2011)) to quantify the integrated deposition rates of the main meteoritic metals in the upper atmospheres of Earth, Mars and Venus, along with the accretion rates of uMMs and CSs. The CABMOD model contains a detailed description of the physical and chemical pro-

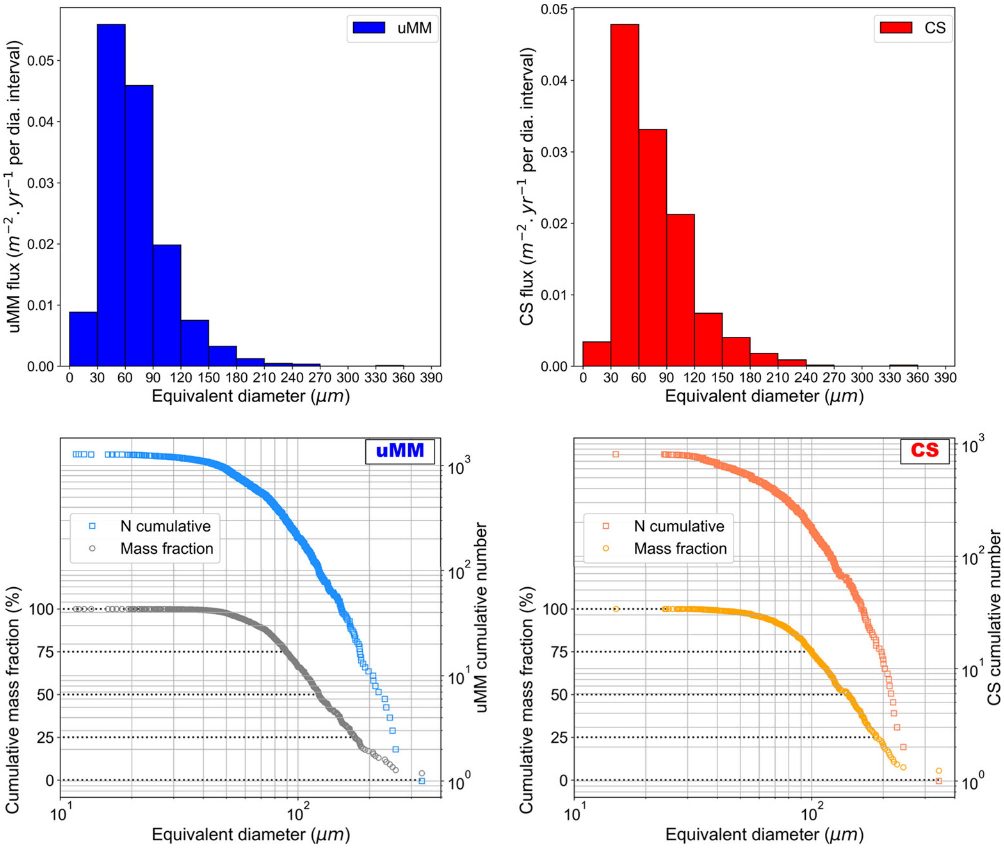

Fig. 3. (Top) Histograms of the uMM (blue) and CS (red) size distributions for the full dataset using equivalent diameter bins of 30 μm. (Bottom) Cumulative number and mass distributions of uMMs (blue and grey) and CSs (red and orange) for the full dataset. The numbers of particles are reported on the right vertical axis and mass fractions on the left vertical axis. (For interpretation of the colours in the figure(s), the reader is referred to the web version of this article.)

cesses of meteoric ablation for a particle of specified mass, velocity and zenith angle entering a planetary atmosphere. Meteoroids are assumed to be spherical with an initial bulk density of 2.2 g.cm^{-3}. (Consolmagno et al., 2008), whereas CSs exhibit a higher density, 3.2 g.cm^{-3} (Kohout et al., 2014). The densities considered in these models are different from that used for the flux calculations from the DC data, however ablation is relatively insensitive to the choice of initial density, e.g. representative particles with a density of 2.2 g.cm^{-3} ablate only 5% more efficiently than those with the same mass and a density of 1.5 g.cm^{-3} (Vondrak et al., 2008). The uncertainties related to the particles density will be considered in the discussion section.

The ZoDy model describes the spatial distribution of position and velocity vectors of meteoroids in the inner solar system for masses between 10^{-3} and 5×10^3 μg (particle diameters from 10 μm to 2 mm), and is calibrated to match various ground-based and space-borne data sets. ZoDy combines products of three major meteoroid source populations in the inner solar system: Jupiter-Family Comets (JFCs), Halley-type Comets (HTCs), and main-belt asteroids (MBAs). In this paper we updated the contributions from these populations using the new CS mass flux from DC collection. The contribution of each meteoroid population to the total mass flux at Earth in turn reflects the total budget of meteoroids in the solar system. Since the work of Nesvorný et al. (2011, 2010), JFCs have been considered the most abundant source of micrometeoroids, dominating 70-90% of Earth's mass flux. The size-frequency distribution (SFD) with which the meteoroids are produced is constrained by Planck satellite observations that only show the overall SFD of the Zodiacal Cloud (Ade et al., 2014), so this mostly provides insight into the SFD of the dominating JFC population and leaves the MBA and HTC SFDs much less constrained. This SFD predominantly influences the detected SFD at Earth. Finally, the collisional lifetime of meteoroids in the inner solar system influences the survivability of meteoroids during their pathway from their sources until they impact Earth; the lifetimes can be constrained using meteor orbit radars (Nesvorný et al., 2011; Pokorný et al., 2014).

3. Results

3.1. The size and mass distributions of cosmic spherules and unmelted micrometeorites

The size distributions of uMMs and CSs from the complete data set are reported in Fig. 3. The uMMs and CSs exhibit a maximum flux in number of particles at $D_{eq} = 50$ μm. The cumulative size distributions and mass fraction derived from the overall data set are also shown in Fig. 3. It is worth noting that a single power law cannot describe these cumulative size distributions.

In Fig. 4, we report the uMM and CS mass influx distributions from the selected melts (dataset #1) and the complete dataset using 30 μm diameter bins (in the upper panels of Fig. 4, grey and orange squares for the selected melts, and blue and red for the complete dataset) along with their fits assuming log-normal laws. The shape of the particle size distribution of the complete data set is compatible with that of the selected melts data (dataset #1), indicating that there is no size bias between the two sets of data (selected and additional).

The sum of the particles' masses relative to the exposure parameter in the selected melts is 2.7 μg.m^{-2}.yr^{-1} for uMMs and 5.2 μg.m^{-2}.yr^{-1} for CSs. These values, which are corrected from Q, provide the absolute mass flux within the 30 to 240 μm diameter range. The log-normal laws were normalized to fit the absolute

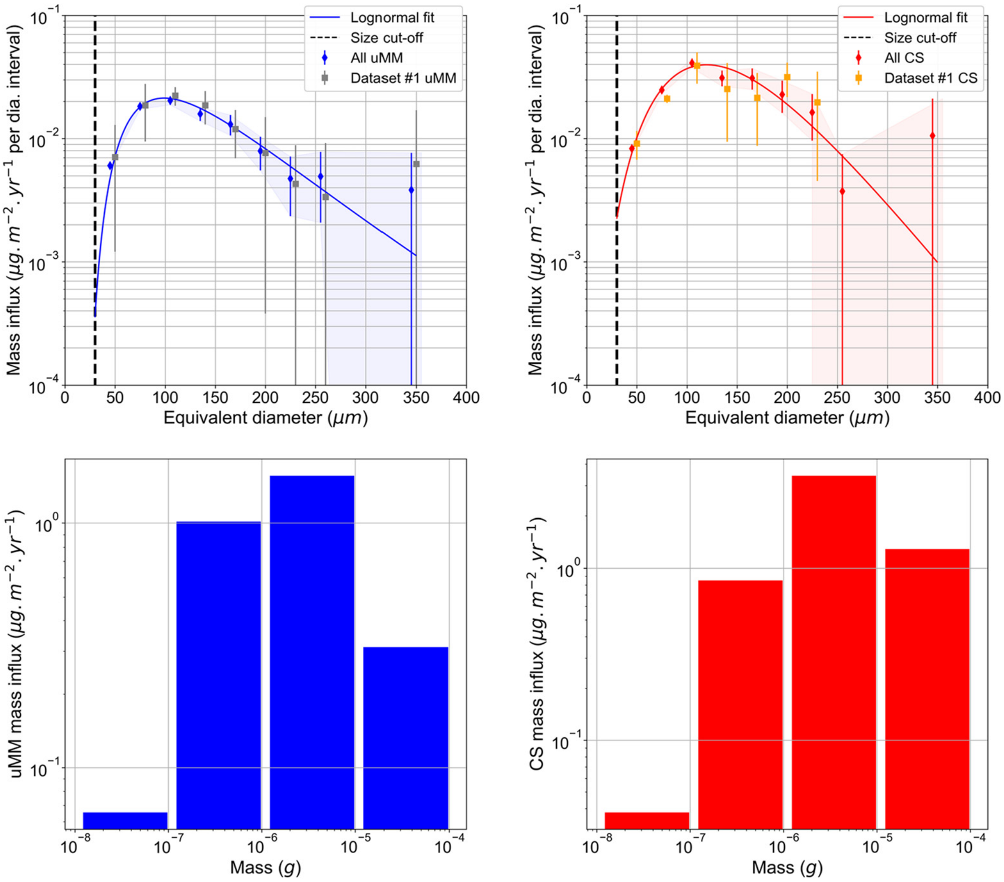

Fig. 4. (Top panels) Size distributions for uMMs (left) and CSs (right) given as mass influxes using 30 μm bins in equivalent diameter. The sizes distributions of uMMs and CSs from the selected melts (Dataset #1) are reported in grey and orange symbols, and that considering the full dataset in blue and red symbols. The uncertainties of the uMM and CS size distributions of the full dataset are outlined in the shaded areas. (bottom panels) Mass distributions for uMMs (left) and CSs (right) deduced from the full dataset, plotted with logarithmic bins in mass.

values from the selected melts (i.e. in the $D_{eq} = 30$ and 240 μm range). Data points from the selected and complete data sets are available in the supplementary table. If one restricts the analysis to melts for which both uMMs and CSs were comprehensively searched for (i.e. excluding DC06-11), as performed e.g. by (Yada et al., 2004), the total mass influx in the 30-240 μm diameter range is 7.7 μg.m^{-2}.yr^{-1}, a value consistent within uncertainties with that found above.

The total mass influx for uMMs and CS over a broader size range can then be obtained by integrating the normalized analytic log-normal fits. Considering a lower cut-off at 12 μm and an upper cut-off at 700 μm, the inferred global values for uMMs and CSs are $\Phi_{\text{uMM}} = 3.0 \pm 1.0$ μg.m^{-2}.yr^{-1} and $\Phi_{\text{CS}} = 5.7 \pm 1.5$ μg.m^{-2}.yr^{-1}, respectively (see Table 1). The errors are derived assuming that the number of influx particles follows Poisson statistics. Extrapolating over the entire Earth's surface, the flux of uMMs is $1,600 \pm 500$ tons.yr^{-1} (4.4 ± 1.4 tons.d^{-1}).

As detailed in the Table 2, about 75% of the uMMs and CSs in the CONCORDIA collection are within the 30-100 μm size range, but they account for less than 30% of the mass influx. uMMs and CSs with diameters ranging from 100 up to 200 μm account for 15% to 20% of the total numbers of particles, whereas they represent about half of the total mass influx. Finally, particles with $D_{eq} > 200$ μm are rare (a few % in numbers) but their contribution to the mass influx is significant, close to 20%. Due to their scarcity, the uncertainties on the contribution of these large particles to the mass influx are higher compared to the contribution in the 30-100 μm range. The extrapolation of the global CSs flux will be discussed below, taking into account the contribution of CSs with diameter greater than 200 μm (see discussion section).

The mass distributions of uMMs and CSs respectively reach their maxima at $D_{eq} = 100$ μm and $D_{eq} = 120$ μm. These sizes correspond to uMMs and CSs of masses around 0.8 μg and 2.7 μg (Fig. 4 bottom panels). For masses above 10 μg, uMMs contribute 10 times less than CSs to the mass influx. The total mass is not sensitive to the broad cut-off considered here (12 −700 μm) as long as their values are chosen sufficiently far from the mass distribution maxima. If one restricts the integration to the range in which particles are actually recovered, i.e. from 30 μm to 350 μm, the mass influxes are respectively 3.0 ± 1.0 μg.m^{-2}.yr^{-1} and 5.6 ± 1.5 μg.m^{-2}.yr^{-1} for uMMs and CSs, i.e. about 2% lower than the total mass flux inferred from the normalised log-normal fit over the whole size range for CSs (12-700 μm).

3.2. Statistical uncertainties related to the exposure parameter

We performed Monte-Carlo simulations to compare the dispersion of the mass influx observed in the different selected melts for both uMMs and CSs with that expected from statistical fluctuations induced by the finite number of micrometeorites collected in each melt. The procedure is detailed in the Annex. We considered a nominal flux Φ_0 given by Φ_{uMM} and Φ_{CS}, carried by particles following the total mass distributions of Fig. 4. The number of particles collected with a sufficiently large S ($S_{ref} = 10^5$ m^2.yr) was taken to be constant, and corresponded to the average number of uMMs and CSs per unit of surface and time within

Table 2
Numbers and mass of uMMs and CSs extracted from selected melts (Dataset#1) and from the complete data set (All) in 4 different size ranges (<30 µm, 30-100 µm, 100-200 µm, >200 µm). The 2 last rows indicate their corresponding contributions to the mass flux, taking into account the collection efficiency (see text). Particles in the 100-200 µm size range make the highest contribution to the mass flux. The uMM and CS distributions from the complete data set are normalized to the selected data set between 30 and 240 µm in diameter. The inferred total mass influx from both uMMs and CSs in the 30-240 µm range and on a global range (12-700 µm) are reported in the last columns. For CSs, we indicate their mass influx considering the Dome C data alone (noted †) and that (noted *) considering the merging of the distribution from this work with that from the SPWW collection (Taylor et al.) for diameters >200 µm (see section 4.1).

D	<30 µm		30 µm-100 µm		100 µm-200 µm		>200 µm		TOTAL	
	Dataset #1	*All*	*Dataset #1*	*All*	*Dataset #1*	*All*	*Dataset #1*	*All*	*Dataset #1*	*All*
N_{CS}	5	23	264	614	55	160	4	11	328	808
N_{uMM}	18	79	532	997	102	194	5	10	657	1280
M_{CS} (µg)	<1	1	112	292	228	624	67	224	407	1141
M_{uMM} (µg)	<1	1	126	243	144	357	65	116	335	717
Flux (with efficiency correction)									30-240 µm	12-700 µm
Φ_{CS} (µg.m^{-2}.yr^{-1}) (fit)	<0.1		1.3		3.3		1.1		5.2	5.7†/7.1*
Φ_{uMM} (µg.m^{-2}.yr^{-1}) (fit)	<0.1		0.9		1.5		0.6		2.7	3.0

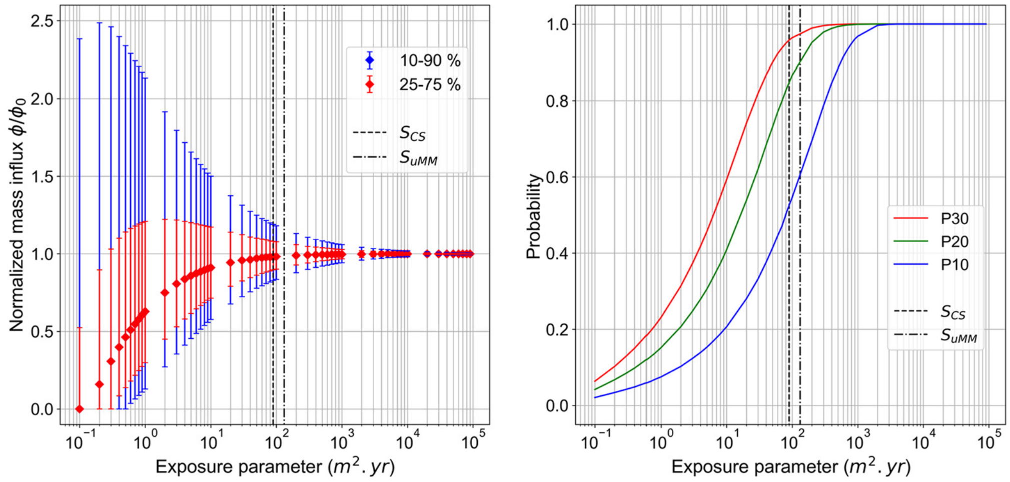

Fig. 5. (left) Variation of the ratio between the measured flux (Φ) and the nominal input flux Φ_0 for different percentile ranges and recovery probability as a function of the exposure parameter S. (right) P30, P20 and P10 are the probabilities (depending on the exposure parameter) that the nominal input flux is estimated to have with less than 30%, 20% or 10% uncertainty, respectively. The vertical dashed lines indicate the exposure parameters S_{CS} and S_{uMM} of the CS and uMM collection from this work.

the 12-700 µm diameter range: $N_{ref}(\mathrm{uMM}) = 4.3$ m^{-2}.yr^{-1} and $N_{ref}(\mathrm{CS}) = 3.6$ m^{-2}.yr^{-1}.

We then simulated the number N_{simu} of collected particles for a set of exposure parameter S. For each simulation, the N_{simu} value was sorted with a binomial law of parameters ($n = N_{ref}$, $p = \frac{S}{S_{ref}}$). The masses M_{simu} of the N_{simu} particles were subsequently sorted according to the global uMM and CS mass distributions reported in Fig. 4 and the numerical measured flux was computed as $\Phi = \frac{M_{simu}}{S}$. For each S, we simulated 10^5 measured fluxes Φ, to infer their median values and the 10-90% and 25-75% variations from the nominal flux Φ_0. The resulting distributions as function of S are presented in the Fig. 5 left panel, for S ranging from 10^{-1} to 10^5 m^2.yr. From these numerical simulations, we derive the probability for a collection of extraterrestrial particles in the 12-700 µm diameter range to estimate the real flux Φ_0 with a relative uncertainty $(\Phi - \Phi_0)/\Phi_0$ smaller than 10%, 20% and 30% (respectively P10, P20 and P30 on Fig. 5, right) as a function of S.

The accuracy of a flux measurement for a given S is monitored by the median Φ/Φ_0 ratio and its variations at the first and last quartile (25-75%) and decile (10-90%). For S lower than 1 m^2.yr, more than 75% of the simulated fluxes have relative uncertainties greater than 30% (Fig. 5, right), preventing reliable statistical measurements being achieved. The left panel in Fig. 5 also demonstrates that collections performed with S lower than a few m^2.yr are subjects to a systematic bias toward an underestimation of the real flux. This feature is due to the fact that, for such low S, the collection statistically misses a significant number of large size particles so that the masses collected tend to be lower than expected from the actual mass distribution. For S greater than a few tens of m^2.yr, this systematic effect becomes negligible (the median Φ/Φ_0 approaches 1), and variations on the measured flux substantially decrease.

For $S \approx 100$ m^2.yr, the probability is about 90% (about 2 σ) that the relative difference between the measured flux Φ and the real flux Φ_0 is less than 20%. We report on Fig. 5 the exposure parameter of the sum of the selected melts (dataset #1) for CSs and uMMs ($S = 89.6$ m^2.yr for CSs and $S = 131.9$ m^2.yr for uMMs). Fig. 5 is helpful for evaluating the statistical biases inherent in a collection for a given exposure parameter.

4. Discussion

Fig. 6 shows the distribution of extraterrestrial particles in near-Earth orbit, derived from hyper-velocity impacts of grains on the *Long Duration Exposure Facility satellite* (LDEF) panel (Love and Brownlee, 1993). Size measurements of the craters caused by high velocity sub-millimetre grain collisions with the panel were used to establish a size distribution of extraterrestrial particles before atmospheric entry. The integrated flux derived from this distribution is about one order of magnitude above that measured in this work. However, ground-based distributions can differ substantially from the pre-atmospheric distribution as a higher mass loss by ablation is expected for larger particles (Vondrak et al., 2008) and partial heating of grains should lead to a mass reduction, shift-

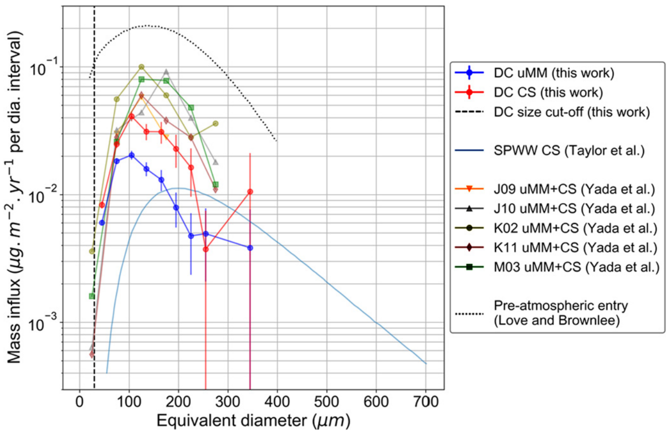

Fig. 6. Distributions of CSs and uMMs obtained from different Antarctic collections. DC uMM and CS: uMM and CS mass distributions from this study. SPWW CS: CS distribution from Taylor et al. (1998). Yada: distributions of mixed uMMs and CSs from Yada et al. (2004). Pre-atmospheric entry distribution of particles are from Love and Brownlee (1993).

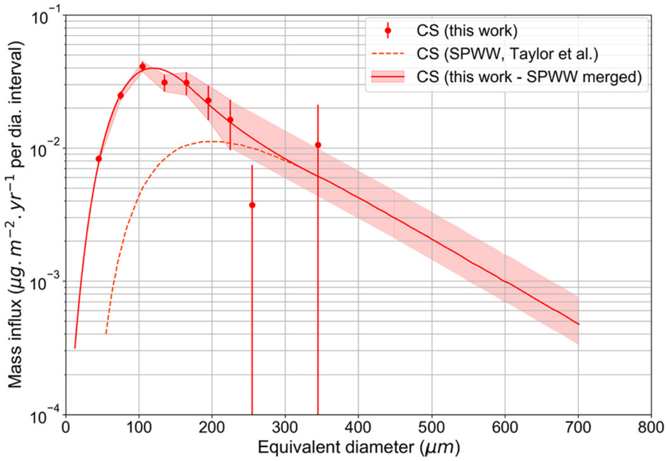

Fig. 7. Global distribution of CSs inferred from the DC data (this work) for $D <$ 200 μm and SPWW (Taylor et al., 1998) data for CS with $D >$ 200 μm. The two datasets consider fully melted particles (CSs) recovered from melted Antarctic snow. The shaded area outlines the uncertainties in the global distribution.

ing the distributions to smaller diameters. The degree of heating experienced by the particles during their atmospheric entry depends on various factors including the initial mass of the particles, their entry angle and velocity. The ablated metallic vapours oxidize and the resulting metal oxides, hydroxides and carbonates condense into nm-sized particles termed meteoric smoke (Plane et al., 2015). These particles are transported by the general atmospheric circulation until eventually deposited at the surface, where their flux can be evaluated by elemental or isotopic measurements (Gabrielli et al. (2004)).

4.1. Comparison with previous flux measurements at the Earth's surface

Several attempts have been made to determine the fluxes of uMMs and CSs in ice caps, deep-sea sediments and surface sediments (Genge et al., 2020; Murrell et al., 1980; Peucker-Ehrenbrink, 2001; Rochette et al., 2008; Suavet et al., 2009; Suttle and Folco, 2020; Taylor et al., 1998; Yada et al., 2004). Each estimation method has its own limitations. Here, we compare the results from the CONCORDIA collection to those obtained under comparable conditions, from Antarctic ice and snow (Taylor et al., 1998; Yada et al., 2004). Yada et al. (2004) performed 5 independent collections in 3 different blue ice fields around the Yamato Mountains (Antarctica). The mass distributions, including both CSs and uMMs, exhibit a maximum between 100 and 200 μm, slightly higher than that determined in the present work for uMMs (100 μm), and in relative agreement with that for CSs (120 μm). The global micrometeorite (CSs and uMMs) flux measured in this work is, within uncertainties, in broad agreement with that measured by Yada et al. (2004) in locations J09 and J01, but is lower than that in the 3 other locations. The variations between the flux measured in distinct blue ice field locations may be explained by the differences in snow accumulation rate and erosion leading to an uncertainty in the S parameter associated with each collection site, and/or by possible variations of the extraterrestrial influx over long periods of time (several 10 kyrs).

Taylor et al. (1998) performed a collection of CSs in the 50-700 μm diameter range from material recovered at the bottom of the South Pole water well (SPWW) of the South Pole Scott-Amundsen station, allowing a large number of particles with sizes mainly above a few hundred μm, up to 700 μm, to be obtained. More recently, Suttle and Folco (2020) reported a flux value and size distributions from thousands of extraterrestrial particles gathered from a collection performed in a sediment trap in the Transantarctic Mountains (TAM). The maximum in the size distributions inferred from both the SPWW and TAM collections is significantly larger (D_{eq} = 200-300 μm) than that reported in this work. The high statistics of both the SPWW and TAM collections for large particles allows a precise size distribution above 200 μm to be inferred. The contribution of smaller particles is more uncertain in these two collections due to lower statistics and uncertainties in the Q value. The transport and settling of the particles within the SPWW geometry and the accumulation in the TAM sediment trap are complex processes resulting in uncertainties in the S and thus on the absolute value of the CS flux. The work presented here is complementary to the SPWW and TAM measurements as it provides an accurate constraint on the absolute value of the flux and on its mass/size distribution for both uMMs and CSs in the lower size range, i.e. below 200 μm.

Only considering the DC data, we infer a total mass flux of $4,500 \pm 1,300$ tons.yr^{-1} (i.e. $1,600 \pm 500$ and $2,900 \pm 800$ tons.yr^{-1} of uMMs and CSs, respectively); however, that estimation should be considered as a lower limit of the flux value, since it does not include large CSs that make a significant contribution to the flux. In Fig. 7 we combine the DC distribution for the low size range with the SPWW distribution for the higher size range (>200 μm), in order to infer a global CS distribution in the overall diameter range (12-700 μm). The uncertainties (the envelope in red) were deduced by shifting vertically the SPWW distribution, but constraining its values to stay consistent with the DC CS experimental points at 195 μm and 225 μm. Such an error range on the absolute value of the SPWW flux is conceivable given the uncertainties on Q and S estimate for this collection. While the flux deduced only from the DC collection yielded a mass flux of $2,900 \pm 800$ tons.yr^{-1} for CSs, taking into account the SPWW data, the integration of the resulting distribution over the total range (12-700 μm) yields a total CS flux of $7.1 \pm^{2.0}_{1.4}$ μg.m^{-2}.yr^{-1} ($3600 \pm^{1000}_{700}$ tons.yr^{-1}) at the Earth's surface, which is a 25% increase of the flux derived from the DC CSs only.

Adding the total contribution of uMMs deduced above, we thus infer that the total mass flux of dust at Earth's surface is $5,200 \pm^{1500}_{1200}$ tons.yr^{-1} ($1,600 \pm 500$ and $3,600 \pm^{1000}_{700}$ tons.yr^{-1} of uMMs and CSs, respectively). This total mass flux of extraterrestrial particles at the Earth's surface is important for many astrophysical and geophysical issues (Peucker-Ehrenbrink and Schmitz, 2001), including the influx of elements on our planet. As far as the carbon (C) flux is concerned, one part reaches the Earth's surface carried by particles that did not suffer from high temperature at atmospheric entry (unaltered C: C_{unalt}) while another part (altered C: C_{alt}) is carried by CSs or uMMs that suffered various degrees of heating at atmospheric entry. C_{unalt} is carried by the fine-grained uMMs (Fg-uMMs) and the Ultra-Carbonaceous Antarctic micrometeorites (UCAMMs) with extreme C concentrations (Dartois et al., 2013, 2018; Duprat et al., 2010; Yabuta et al., 2017). The Fg-uMM mass flux represents ∼40% of the uMM flux and their C concentration, [C], is similar to that in carbonaceous chondritic material. Considering an average [C] = (3 ± 2) wt% (Matrajt et al., 2003), their global Carbon flux is (19 ± 13) tons.yr^{-1}. The C/Si ratio in UCAMMs varies over a wide range from 10 to 10^3 (Dartois et al., 2018) and thus an average is [C] = (60 ± 30) wt%. In the CONCORDIA collection, the mass of UCAMM is 0.7% of that of uMMs and so, their associated C flux is (7 ± 3) tons.yrs^{-1}. The resulting global flux of C_{unalt} is thus (26 ± 16) tons.yr^{-1}. Considering an average [C] of (0.6 ± 0.4) wt% for CSs and (1 ± 0.8) wt% for non-Fg uMMs (Matrajt et al., 2003), the inferred total flux of C_{alt} is (31 ± 22) tons.yr^{-1}, with ∼70% carried by CSs and ∼30% by partially heated uMMs. Given these uncertainties, the total C flux shows a quite large range of variation (20-100 tons.yr^{-1}), with up to half of this C flux is in form of C_{unalt}. Noticeably, the flux of C from UCAMMs represents about 25% of the C_{unalt} flux, indicating that a substantial part of the interplanetary organics reaching Earth surface can originate from the specific cometary reservoir that is the parent body of UCAMMs.

4.2. Comparison with dynamical and atmospheric entry simulations

The fluxes measured in this work together with the ZoDy and CABMOD models produce new constraints on the total dust flux encountered by Earth and the fraction that is ablated at atmospheric entry. For each dust population (JFCs, MBAs, and HTCs), particles are Monte-Carlo selected from the size and velocity distributions predicted by the ZoDy model. The CABMOD model then provides their Na and Fe ablation rates, and the size of the residual CSs (if complete ablation does not occur). To determine the mass contribution of the three cosmic dust sources, we follow the fitting procedure developed by Carrillo-Sánchez et al. (2020a, 2020b), using global mass input rates of Na and Fe in the Earth's atmosphere (above 87.5 km) of 0.3 ± 0.1 tons.d^{-1} and 2.3 ± 1.1 tons.d^{-1} (Gardner et al., 2014), respectively, and the CS flux inferred here (see Annex). Table S1 (Supporting Information) lists the partitioning of the mass influx from the three dust sources into uMMs, CSs, and the total ablated mass (the main elemental components are also shown). JFCs are the main mass contributor (>60%); the contribution from MBAs is lower (20%), about twice the previous estimate by Carrillo-Sánchez et al. (2020a, 2020b).

Fig. 8 shows that in the D_{eq} = 100-350 μm range, ZoDy dynamical simulations satisfactorily account for the proportion of CSs and uMMs determined from the CONCORDIA collection. In order to compare the measurements with the simulations, we indicate in Fig. 8 the range of variation (blue envelope) of the uMM mass distribution for density values between 0.8 g.cm^{-3} and 2.2 g.cm^{-3}, representing the cometary and asteroidal end-members discussed in Section 2.2. Considering these two end cases, the resulting average global uMM flux on Earth would be shifted by about 45%, to 800 or 2,400 tons.yr^{-1}, for average densities of 0.8 g.cm^{-3} and 2.2 g.cm^{-3}, respectively. In contrast, CABMOD-ZoDy predicts an overall uMM influx of 5,000 tons.yr^{-1} in the size range between 30 μm and 360 μm (see Table S1). As a result, the CS:uMM ratio of the CONCORDIA dataset in this size range (=2.0) is 3.4 times larger than the CABMOD-ZoDy estimate.

A marked discrepancy between the experimental and modelled distributions is observed for D_{eq} < 100 μm (Fig. 8), where the number of particles collected is much lower than that expected from the model. This difference may be explained by the occurrence of extremely fragile particles that fragment during atmospheric entry, and/or by the fact that particles in the smallest size range cannot be collected efficiently with the state-of-the-art collection techniques. An alternative explanation is that there is an underestimated process in the orbital evolution of dust, which leads to a lower number of small particles entering the Earth's atmosphere. However, meteoroids migrate toward Earth-crossing orbits via Poynting-Robertson drag (e.g., Burns et al., 1979), where the migration speed scales as $1/D_{eq}$. Since smaller meteoroids migrate faster, they are always more likely to survive the migration. Therefore, changing the collisional lifetime in the model will not diminish the number (or mass contribution) of small meteoroids but will mostly affect the relative contribution of larger meteoroids.

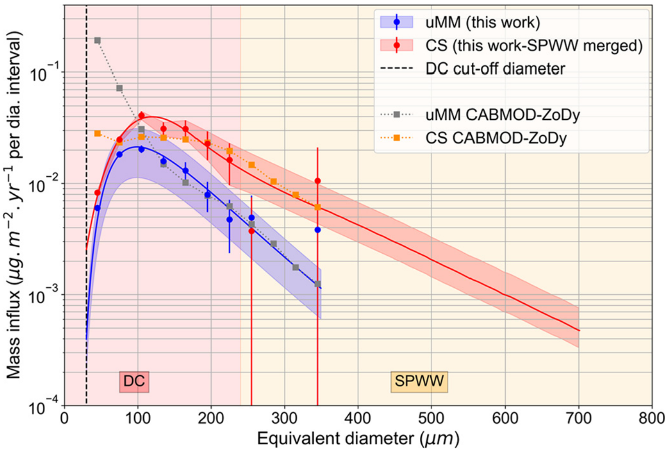

Fig. 8. Global mass influx distributions for uMMs (blue) and CSs (red) compared to the CABMOD-ZoDy estimate of uMMs (grey) and CSs (orange) at the Earth's surface. The blue envelope indicates the impact of the mass density of uMMs on the uMM mass influx distribution, the lower and upper limits of the envelope correspond to uMM average densities of 0.8 and 2.2 g.cm^{-3}.

With the hypotheses considered in this work, the inferred total dust mass before atmospheric entry deduced from the CABMOD-ZoDy modelling is ∼15,000 tons.yr^{-1} (∼40 tons.d^{-1}). Because of the difference between the CABMOD-ZoDy modelling and the measurements of uMMs flux below 100 μm, an uncertainty remains regarding the absolute value of this flux. Since the contribution of uMMs and CSs below 100 μm to the mass flux measured at DC is less than 30% of the total, the total dust mass before atmospheric entry should be in the range 10,000-20,000 tons.yr^{-1}, in agreement with previous studies (Plane (2012), Love and Brownlee, 1993). The flux of unaltered carbon deduced considering the progressive pyrolysis of carbon at atmospheric entry (Carrillo-Sánchez et al. (2020a, 2020b)), is ∼12 tons.yr^{-1} (see Annex) that is compatible with the lower limit of that inferred from the CONCORDIA collection.

5. Conclusion

We performed several independent collections of micrometeorites from ultra-clean snow samples in the vicinity of the CONCORDIA Station at Dome C. The regular snow accumulation rate at Dome C allows to control the related exposure parameter (in m^2.yr) and the exceptional cleanliness of Dome C surface snow allows fragile particles to be recovered with high efficiency. 1280 uMMs and 808 CSs were collected from snow and subsequently characterized by conventional scanning electron microscopy techniques. This collection provides new constraints on size distributions of extraterrestrial dust reaching the Earth's surface, down to a size of 30 μm. The resulting mass distributions show well-defined maxima at D_{eq} = 100 μm for uMMs and D_{eq} = 120 μm for CSs, slightly below estimates from previous studies. From four independents melts analyzed, we measured a total mass flux carried by particles in the 30-240 μm diameter range of 2.7 μg.m^{-2}.yr^{-1} for uMMs and 5.2 μg.m^{-2}yr^{-1} for CSs. The mass distributions were fitted with log-normal distributions. Comparison with previous measurements up to higher sizes (Taylor et al., 1998) enabled extrapolation to a global flux covering the 12-700 μm diameter range at Earth's surface of $(1,600 \pm 500)$ and $(3,600 \pm {}^{1000}_{700})$ tons.yr^{-1} for uMMs and CSs, respectively. The corresponding flux in carbon carried by these particles ranges from 20 to 100 tons.yr^{-1}. About 25% of the flux reaching Earth's surface as unaltered C is carried by particles with extreme carbon concentration (UCAMMs) originating from the cometary reservoir. We performed numerical simulations that can be used to evaluate the statistical uncertainties of future collections considering a wide range of exposure parameters from 0.1 to 10^5 m^2.yr.

New calculations were performed using the CABMOD-ZoDy model constrained by the CONCORDIA uMM and CS flux. These numerical simulations confirm that a majority of the incoming extraterrestrial flux are expected to originate from Jupiter family comets. The CABMOD-ZoDy model satisfactorily reproduces the CONCORDIA mass distribution of CSs and uMMs above 100 μm at the Earth's surface, and the total dust mass input before atmospheric entry is about 15,000 tons.yr^{-1}. Below 100 μm, the model calculations predict a flux of uMMs substantially greater than that measured in the CONCORDIA collection. This suggests several possibilities: the existence of highly fragile particles that would not be collected with the collection protocol in Dome C snow; fragmentation removal of a significant number of small particles before atmospheric entry; or that the actual amount of small interplanetary particles at 1 AU may be smaller than expected.

CRediT authorship contribution statement

J. Rojas: Writing – original draft, Writing – review & editing, Methodology. **J. Duprat:** Supervision, Writing – original draft, Writing – review & editing, Data curation, Field work, Funding acquisition. **C. Engrand:** Writing – review & editing, Data curation, Field work, Funding acquisition. **E. Dartois:** Writing – review & editing, Data curation, Field work. **L. Delauche:** Data curation, Field work. **M. Godard:** Writing – review & editing, Data curation, Field work. **M. Gounelle:** Writing – review & editing, Field work. **J.D. Carrillo-Sánchez:** Writing – original draft, Writing – review & editing, Data curation, Methodology. **P. Pokorný:** Writing – original draft, Writing – review & editing, Data curation, Methodology, **J.M.C. Plane:** Writing – original draft, Writing – review & editing, Data curation, Methodology.

Declaration of competing interest

The authors declare that they have no known competing financial interests or personal relationships that could have appeared to influence the work reported in this paper.

Acknowledgements

This work was performed at CONCORDIA Station (project #1120) and was supported by the French Polar Institute (IPEV). We are very grateful to IPEV for financial support and to IPEV and PNRA staff for logistical help. E. Le Meur kindly provided us helpful information on accumulation rates central Antarctic regions. We thank the anonymous referees for their thoughtful and constructive suggestions. This work was financially supported by ANR (Project COMETOR 18-CE31-0011), Region Ile de France (DIM-ACAV and ACAV+), PNP/INSU, CNES, IN2P3 and Labex P2IO. The CABMOD-ZoDy work was supported by the UK NERC (Grant Number NE/P001815/1) and NASA ISFM awards.

Appendix A. Supplementary material

Supplementary material related to this article can be found online at https://doi.org/10.1016/j.epsl.2021.116794. These data include the Google map of the most important areas described in this article.

References

Ade, P.A.R., Aghanim, N., Alves, M.I.R., Armitage-Caplan, C., Arnaud, M., Ashdown, M., Atrio-Barandela, F., Aumont, J., Aussel, H., Baccigalupi, C., Banday, A.J., Barreiro, R.B., Barrena, R., Bartelmann, M., Bartlett, J.G., Bartolo, N., Basak, S., Battaner, E., Battye, R., Benabed, K., Benoît, A., Benoit-Lévy, A., Bernard, J.-P., Bersanelli, M., Bertincourt, B., Bethermin, M., Bielewicz, P., Bikmaev, I., Blanchard, A., Bobin, J., Bock, J.J., Böhringer, H., Bonaldi, A., Bonavera, L., Bond, J.R., Borrill, J., Bouchet, F.R., Boulanger, F., Bourdin, H., Bowyer, J.W., Bridges, M., Brown, M.L., Bucher, M., Burenin, R., Burigana, C., Butler, R.C., Calabrese, E., Cappellini, B., Cardoso, J.-F., Carr, R., Carvalho, P., Casale, M., Castex, G., Catalano, A., Challinor, A., Chamballu, A., Chary, R.-R., Chen, X., Chiang, H.C., Chiang, L.-Y., Chon, G., Christensen, P.R., Churazov, E., Church, S., Clemens, M., Clements, D.L., Colombi, S., Colombo, L.P.L., Combet, C., Comis, B., Couchot, F., Coulais, A., Crill, B.P., Cruz, M., Curto, A., Cuttaia, F., Da Silva, A., Dahle, H., Danese, L., Davies, R.D., Davis, R.J., de Bernardis, P., de Rosa, A., de Zotti, G., Déchelette, T., Delabrouille, J., Delouis, J.-M., Démoclès, J., Désert, F.-X., Dick, J., Dickinson, C., Diego, J.M., Dolag, K., Dole, H., Donzelli, S., Doré, O., Douspis, M., Ducout, A., Dunkley, J., Dupac, X., Efstathiou, G., Elsner, F., Enßlin, T.A., Eriksen, H.K., Fabre, O., Falgarone, E., Falvella, M.C., Fantaye, Y., Fergusson, J., Filliard, C., Finelli, F., Flores-Cacho, I., Foley, S., Forni, O., Fosalba, P., Frailis, M., Fraisse, A.A., Franceschi, E., Freschi, M., Fromenteau, S., Frommert, M., Gaier, T.C., Galeotta, S., Gallegos, J., Galli, S., Gandolfo, B., Ganga, K., Gauthier, C., Génova-Santos, R.T., Ghosh, T., Giard, M., Giardino, G., Gilfanov, M., Girard, D., Giraud-Héraud, Y., Gjerløw, E., González-Nuevo, J., Górski, K.M., Gratton, S., Gregorio, A., Gruppuso, A., Gudmundsson, J.E., Haissinski, J., Hamann, J., Hansen, F.K., Hansen, M., Hanson, D., Harrison, D.L., Heavens, A., Helou, G., Hempel, A., Henrot-Versillé, S., Hernández-Monteagudo, C., Herranz, D., Hildebrandt, S.R., Hivon, E., Ho, S., Hobson, M., Holmes, W.A., Hornstrup, A., Hou, Z., Hovest, W., Huey, G., Huffenberger, K.M., Hurier, G., Ilić, S., Jaffe, A.H., Jaffe, T.R., Jasche, J., Jewell, J., Jones, W.C., Juvela, M., Kalberla, P., Kangaslahti, P., Keihänen, E., Kerp, J., Keskitalo, R., Khamitov, I., Kiiveri, K., Kim, J., Kisner, T.S., Kneissl, R., Knoche, J., Knox, L., Kunz, M., Kurki-Suonio, H., Lacasa, F., Lagache, G., Lähteenmäki, A., Lamarre, J.-M., Langer, M., Lasenby, A., Lattanzi, M., Laureijs, R.J., Lavabre, A., Lawrence, C.R., Le Jeune, M., Leach, S., Leahy, J.P., Leonardi, R., León-Tavares, J., Leroy, C., Lesgourgues, J., Lewis, A., Li, C., Liddle, A., Liguori, M., Lilje, P.B., Linden-Vørnle, M., Lindholm, V., López-Caniego, M., Lowe, S., Lubin, P.M., Macías-Pérez, J.F., MacTavish, C.J., Maffei, B., Maggio, G., Maino, D., Mandolesi, N., Mangilli, A., Marcos-Caballero, A., Marinucci, D., Maris, M., Marleau, F., Marshall, D.J., Martin, P.G., Martínez-González, E., Masi, S., Massardi, M., Matarrese, S., Matsumura, T., Matthai, F., Maurin, L., Mazzotta, P., McDonald, A., McEwen, J.D., McGehee, P., Mei, S., Meinhold, P.R., Melchiorri, A., Melin, J.-B., Mendes, L., Menegoni, E., Mennella, A., Migliaccio, M., Mikkelsen, K., Millea, M., Miniscalco, R., Mitra, S., Miville-Deschênes, M.-A., Molinari, D., Moneti, A., Montier, L., Morgante, G., Morisset, N., Mortlock, D., Moss, A., Munshi, D., Murphy, J.A., Naselsky, P., Nati, F., Natoli, P., Negrello, M., Nesvadba, N.P.H., Netterfield, C.B., Nørgaard-Nielsen, H.U., North, C., Noviello, F., Novikov, D., Novikov, I., O'Dwyer, I.J., Orieux, F., Osborne, S., O'Sullivan, C., Oxborrow, C.A., Paci, F., Pagano, L., Pajot, F., Paladini, R., Pandolfi, S., Paoletti, D., Partridge, B., Pasian, F., Patanchon, G., Paykari, P., Pearson, D., Pearson, T.J., Peel, M., Peiris, H.V., Perdereau, O., Perotto, L., Perrotta, F., Pettorino, V., Piacentini, F., Piat, M., Pierpaoli, E., Pietrobon, D., Plaszczynski, S., Platania, P., Pogosyan, D., Pointecouteau, E., Polenta, G., Ponthieu, N., Popa, L., Poutanen, T., Pratt, G.W., Prézeau, G., Prunet, S., Puget, J.-L., Pullen, A.R., Rachen, J.P., Racine, B., Rahlin, A., Räth, C., Reach, W.T., Rebolo, R., Reinecke, M., Remazeilles, M., Renault, C., Renzi, A., Riazuelo, A., Ricciardi, S., Riller, T., Ringeval, C., Ristorcelli, I., Robbers, G., Rocha, G., Roman, M., Rosset, C., Rossetti, M., Roudier, G., Rowan-Robinson, M., Rubiño-Martín, J.A., Ruiz-Granados, B., Rusholme, B., Salerno, E., Sandri, M., Sanselme, L., Santos, D., Savelainen, M., Savini, G., Schaefer, B.M., Schiavon, F., Scott, D., Seiffert, M.D., Serra, P., Shellard, E.P.S., Smith, K., Smoot, G.F., Souradeep, T., Spencer, L.D., Starck, J.-L., Stolyarov, V., Stompor, R., Sudiwala, R., Sunyaev, R., Sureau, F., Sutter, P., Sutton, D., Suur-Uski, A.-S., Sygnet, J.-F., Tauber, J.A., Tavagnacco, D., Taylor, D., Terenzi, L., Texier, D., Toffolatti, L., Tomasi, M., Torre, J.-P., Tristram, M., Tucci, M., Tuovinen, J., Türler, M., Tuttlebee, M., Umana, G., Valenziano, L., Valiviita, J., Van Tent, B., Varis, J., Vibert, L., Viel, M., Vielva, P., Villa, F., Vittorio, N., Wade, L.A., Wandelt, B.D., Watson, C., Watson, R., Wehus, I.K., Welikala, N., Weller, J., White, M., White, S.D.M., Wilkinson, A., Winkel, B., Xia, J.-Q., Yvon, D., Zacchei, A., Zibin, J.P., Zonca, A., 2014. Planck 2013 results. I. Overview of products and scientific results. Astron. Astrophys. 571, A1.

Burns, J.A., Lamy, P.L., Soter, S., 1979. Radiation forces on small particles in the solar system. Icarus 40, 1.

Carrillo-Sánchez, J.D., Nesvorný, D., Pokorný, P., Janches, D., Plane, J.M.C., 2016. Sources of cosmic dust in the Earth's atmosphere. Geophys. Res. Lett. 43, 11,979–11,986.

Carrillo-Sánchez, J.D., Gómez-Martín, J.C., Bones, D.L., Nesvorný, D., Pokorný, P., Benna, M., Flynn, G.J., Plane, J.M.C., 2020a. Cosmic dust fluxes in the atmospheres of Earth, Mars, and Venus. Icarus 335, 113395.

Carrillo Sánchez, J.D., Bones, D., Douglas, K.M., Flynn, G.J., Wirick, S., Fegley, B., Araki, T., Kaulich, B., Plane, J.M.C., 2020b. Injection of meteoric phosphorus into planetary atmospheres. Planet. Space Sci. 187, 104926.

Consolmagno, G.J., Britt, D.T., Macke, R.J., 2008. The significance of meteorite density and porosity. Chem. Erde 68, 1–29.

Dartois, E., Engrand, C., Brunetto, R., Duprat, J., Pino, T., Quirico, E., Remusat, L., Bardin, N., Briani, G., Mostefaoui, S., Morinaud, G., Crane, B., Szwec, N., Delauche, L., Jamme, F., Sandt, C., Dumas, P., 2013. UltraCarbonaceous Antarctic micrometeorites, probing the Solar System beyond the nitrogen snow-line. Icarus 224, 243–252.

Dartois, E., Engrand, C., Duprat, J., Godard, M., Charon, E., Delauche, L., Sandt, C., Borondics, F., 2018. Dome C ultracarbonaceous Antarctic micrometeorites. Infrared and Raman fingerprints. Astron. Astrophys. 609.

Delmonte, B., Petit, J.R., Andersen, K.K., Basile-Doelsch, I., Maggi, V., Lipenkov, V.Y., 2004. Dust size evidence for opposite regional atmospheric circulation changes over East Antarctica during the last climatic transition. Clim. Dyn. 23, 427.

Duprat, J., Dobrică, E., Engrand, C., Aléon, J., Marrocchi, Y., Mostefaoui, S., Meibom, A., Leroux, H., Rouzaud, J.-N., Gounelle, M., Robert, F., 2010. Extreme deuterium excesses in ultracarbonaceous micrometeorites from central Antarctic snow. Science 328, 742–745.

Flynn, G.J., Sutton, S.R., 1991. Cosmic dust particle densities: evidence for two populations of stony micrometeorites. Proc. Lunar Planet. Sci. Conf. 21, 541.

Frezzotti, M., Pourchet, M., Flora, O., Gandolfi, S., Gay, M., Urbini, S., Vincent, C., Becagli, S., Gragnani, R., Poposito, M., Severi, M., Traversi, R., Udisti, R., Fily, M., 2005. Spatial and temporal variability of snow accumulation in East Antarctica from traverse data. J. Glaciol. 51, 113–124.

Fulle, M., Della Corte, V., Rotundi, A., Rietmeijer, F.J.M., Green, S.F., Weissman, P., Accolla, M., Colangeli, L., Ferrari, M., Ivanovski, S., Lopez-Moreno, J.J., Epifani, E.M., Morales, R., Ortiz, J.L., Palomba, E., Palumbo, P., Rodriguez, J., Sordini, R., Zakharov, V., 2016. Comet 67P/Churyumov-Gerasimenko preserved the pebbles that formed planetesimals. Mon. Not. R. Astron. Soc. 462, S132.

Gabrielli, P., Barbante, C., Plane, J.M.C., Varga, A., Hong, S., Cozzi, G., Gaspari, V., Planchon, F.A.M., Cairns, W., Ferrari, C., Crutzen, P., Cescon, P., Boutron, C.F., 2004. Meteoric smoke fallout over the Holocene epoch revealed by iridium and platinum in Greenland ice. Nature 432, 1011–1014.

Gardner, C.S., Liu, A.Z., Marsh, D.R., Feng, W.H., Plane, J.M.C., 2014. Inferring the global cosmic dust influx to the Earth's atmosphere from lidar observations of the vertical flux of mesospheric Na. J. Geophys. Res. Space Phys. 119, 10.

Genge, M.J., Van Ginneken, M., Suttle, M.D., 2020. Micrometeorites: insights into the flux, sources and atmospheric entry of extraterrestrial dust at Earth. Planet. Space Sci. 187.

Hauser, M.G., Gillett, F.C., Low, F.J., Gautier, T.N., Beichman, C.A., Neugebauer, G., Aumann, H.H., Baud, B., Boggess, N., Emerson, J.P., Houck, J.R., Soifer, B.T., Walker, R.G., 1984. IRAS observations of the diffuse infrared background. Astrophys. J. 278, L15.

Joswiak, D.J., Brownlee, D.E., Pepin, R.O., Schlutter, D.J., 2007. Densities and mineralogy of cometary and asteroidal interplanetary dust particles collected in the stratosphere. In: Dust in Planetary Systems, p. 141.

Kohout, T., Kallonen, A., Suuronen, J.P., Rochette, P., Hutzler, A., Gattacceca, J., Badjukov, D.D., Skála, R., Böhmová, V., Čuda, J., 2014. Density, porosity, mineralogy, and internal structure of cosmic dust and alteration of its properties during high-velocity atmospheric entry. Meteorit. Planet. Sci. 49, 1157–1170.

Le Meur, E., Magand, O., Arnaud, L., Fily, M., Frezzotti, M., Cavitte, M., Mulvaney, R., Urbini, S., 2018. Spatial and temporal distributions of surface mass balance between Concordia and Vostok stations, Antarctica, from combined radar and ice core data: first results and detailed error analysis. Cryosphere 12, 1831–1850.

Love, S.G., Brownlee, D.E., 1993. A direct measurement of the terrestrial mass accretion rate of cosmic dust. Science 262, 550–553.

Love, S.G., Joswiak, D.J., Brownlee, D.E., 1994. Densities of stratospheric micrometeorites. Icarus 111, 227.

Matrajt, G., Taylor, S., Flynn, G., Brownlee, D., Joswiak, D., 2003. A nuclear microprobe study of the distribution and concentration of carbon and nitrogen in Murchison and Tagish Lake meteorites, Antarctic micrometeorites, and IDPs: implications for astrobiology. Meteorit. Planet. Sci. 38, 1585–1600.

Murray, J., Renard, A.F., 1891. Report on the Scientific Results of the Voyage of HMS Challenger during the Years 1873-76, Part 3, Deep-Sea Deposits. HMSO.

Murrell, M.T., Davis, P.A., Nishiizumi, K., Millard, H.T., 1980. Deep-sea spherules from Pacific clay: mass distribution and influx rate. Geochim. Cosmochim. Acta 44, 2067–2074.

Nesvorný, D., Janches, D., Vokrouhlický, D., Pokorný, P., Bottke, W.F., Jenniskens, P., 2011. Dynamical model for the zodiacal cloud and sporadic meteors. Astrophys. J. 743, 129.

Nesvorný, D., Jenniskens, P., Levison, H.F., Bottke, W.F., Vokrouhlický, D., Gounelle, M., 2010. Cometary origin of the zodiacal cloud and carbonaceous micrometeorites. Implications for hot debris disks. Astrophys. J. 713, 816.

Peucker-Ehrenbrink, B., 2001. Iridium and osmium as tracers of extraterrestrial matter in marine sediments. In: Accretion of Extraterrestrial Matter Throughout Earth's History, pp. 163–178.

Peucker-Ehrenbrink, B., Ravizza, G., Winckler, G., 2016. Geochemical tracers of extraterrestrial matter in sediments. Elements 12, 191–196.

Peucker-Ehrenbrink, B., Schmitz, B., 2001. Accretion of Extraterrestrial Matter Throughout Earth's History.

Plane, J.M.C., 2012. Cosmic dust in the Earth's atmosphere. Chem. Soc. Rev. 41, 6507–6518.

Plane, J.M.C., Feng, W., Dawkins, E.C.M., 2015. The mesosphere and metals: chemistry and changes. Chem. Rev. 115, 4497–4541.

Pokorný, P., Vokrouhlický, D., Nesvorný, D., Campbell-Brown, M., Brown, P., 2014. Dynamical model for the toroidal sporadic meteors. Astrophys. J. 789, 25.

Rochette, P., Folco, L., Suavet, C., van Ginneken, M., Gattacceca, J., Perchiazzi, N., Braucher, R., Harvey, R., 2008. Micrometeorites from the transantarctic mountains. Proc. Natl. Acad. Sci. USA 105, 18206–18211.

Suavet, C., Rochette, P., Kars, M., Gattacceca, J., Folco, L., Harvey, R.P., 2009. Statistical properties of the Transantarctic Mountains (TAM) micrometeorite collection. Polar Sci. 3, 100.

Suttle, M.D., Folco, L., 2020. The extraterrestrial dust flux: size distribution and mass contribution estimates inferred from the Transantarctic Mountains (TAM) micrometeorite collection. JGR Planets 125.

Sykes, M.V., 1990. Zodiacal dust bands: their relation to asteroid families. Icarus 85, 267.

Taylor, S., Lever, J.H., Harvey, R.P., 1998. Accretion rate of cosmic spherules measured at the South Pole. Nature 392, 899–903.

Vondrak, T., Plane, J.M.C., Broadley, S., Janches, D., 2008. A chemical model of meteoric ablation. Atmos. Chem. Phys. 8, 7015–7031.

Yabuta, H., Noguchi, T., Itoh, S., Nakamura, T., Miyake, A., Tsujimoto, S., Ohashi, N., Sakamoto, N., Hashiguchi, M., Abe, K.-i., Okubo, A., Kilcoyne, A.L.D., Tachibana, S., Okazaki, R., Terada, K., Ebihara, M., Nagahara, H., 2017. Formation of an ultracarbonaceous Antarctic micrometeorite through minimal aqueous alteration in a small porous icy body. Geochim. Cosmochim. Acta 214, 172–190.

Yada, T., Nakamura, T., Takaoka, N., Noguchi, T., Terada, K., Yano, H., Nakazawa, T., Kojima, H., 2004. The global accretion rate of extraterrestrial materials in the last glacial period estimated from the abundance of micrometeorites in Antarctic glacier ice. Earth Planets Space 56, 67–79.